Final Report for YSU Center of Transportation and Materials Engineering (YSU CTME)

Project Title: Study of Low-Temperature Active Rare-Earth Oxide Catalysts for Automotive Exhaust Clean-up

Prepared by: Ruigang Wang (PI)
Department of Chemistry
Youngstown State University

2/11/2014

Summary: We report a facile one–pot synthesis of $Ce_xZr_{1-x}O_2$ ($0 \leq x \leq 1$) solid solution nanocrystals using hydrothermal reactions. A direct formation of oxide solid solutions in aqueous solution under pressure at low temperatures was clearly revealed by X-ray diffraction, Raman spectroscopy, and chemical composition analysis of individual nanocrystals using energy dispersive X-ray spectroscopy in scanning transmission electron microscopy mode. Chemisorption behavior of the synthesized nanocrystals was characterized using hydrogen temperature programmed reduction, which showed a superior low-temperature activity in $Ce_xZr_{1-x}O_2$ ($0<x<1$) compared to pure CeO_2. Furthermore, we investigated the thermal stability of the prepared $Ce_{0.5}Zr_{0.5}O_2$ at high temperatures (900^oC-1400^oC) under oxidation and reduction atmosphere. The effect of varying conditions of heat-treatment has given information on the phase transformation in $Ce_{0.5}Zr_{0.5}O_2$ from psudocubic to tetragonal structure under oxidation atmosphere, and to pyrochlore structure under reduction atmosphere. With funds from this grant, Youngstown State University has purchased a TA Q50 thermogravimetric analyzer (TGA) for thermal stability and reducibility test of the synthesized oxide nanocatalysts. PI has been involved in the purchase and installation of the instruments. The instrument was fully operational in the spring of 2012 and has so far been used for student research. Out of this project, two refereed and three proceeding papers were published, along with several oral presentations made by PI and students.

1. Instrument Acquisition

A new TA Q50 thermogravimetric analyzer (TGA) was purchased and installed in the PI's group, located at the Department of Chemistry, shown in Figure 1. The purchase of this instrument is in part supported by DoT-CTME project. Acquisition of the state-of-the-art analytical instruments benefits our program not only by providing new research capabilities currently unavailable to us, but also in student learning and courses/labs. Because of our strong "hands-on" access policy regarding graduate and undergraduate access to *all* research-grade equipment in our department, our students are the primary beneficiaries of the acquisition. We used this instrument to study the thermal stability and reducibility of rare-earth oxides that we made in our lab.

Figure 1. A TA Q50 TGA funded in the project for the thermal stability and reducibility characterization of oxide nanocatalysts.

2. Major Accomplishments

One-pot hydrothermal synthesis of $Ce_xZr_{1-x}O_2$ ($0 \leq x \leq 1$)

Figure 2 shows the XRD patterns for a series of $Ce_xZr_{1-x}O_2$ ($0 \leq x \leq 1$) from pure CeO_2 and ZrO_2 to mixed oxides (or solid solutions) nanopowders, prepared via hydrothermal reactions at 150 ^{o}C with a dwell time 48 hrs. The diffraction peaks of pure CeO_2 and ZrO_2 were indexed as face-centered cubic fluorite structured CeO_2 (JCPDS file 34-0394) and monoclinic ZrO_2 (JCPDS 37-1484) with lattice parameters of a=5.156 Å, b=5.191 Å, c=5.304 Å, respectively. The XRD patterns of the mixed $Ce_xZr_{1-x}O_2$ ($0<x<1$) did not show any extra diffraction peaks due to the doping ZrO_2 component from x=0.9 up to x=0.2 but the presence of Zr in individual nanocrytals was evidenced by EDX analysis with a focused electron probe in STEM mode and XRF compositional analysis. The diffraction peaks in mixed oxides were indexed using cubic CeO_2, although the peak positions were shifted to higher diffraction angle when doping more ZrO_2,

compared to standard cubic CeO_2. We attribute this shift to the difference in ionic size between Ce^{4+}(0.97 Å) and Zr^{4+}(0.84 Å), according to the Bragg's law ($2dsin\theta = n\lambda$, where d is the spacing between the planes in the atomic lattice, θ is the diffraction angle, n is an integer, and λ is the wavelength of incident X-ray wavelength). Since Zr^{4+} has a smaller ionic size compared to Ce^{4+}, doping with Zr^{4+} in CeO_2 lattice will result in a shrinked lattice (smaller d spacing and lattice constant). According to the Bragg's law, the diffraction angle θ will increase with the increasing ZrO_2 concentration in $Ce_xZr_{1-x}O_2$ (0≤x≤1). When ZrO_2 concentration is higher than 80% (x<0.2 in $Ce_xZr_{1-x}O_2$), phase separation appears for the $Ce_{0.1}Zr_{0.9}O_2$ sample which is consistent with CeO_2-ZrO_2 phase diagram.
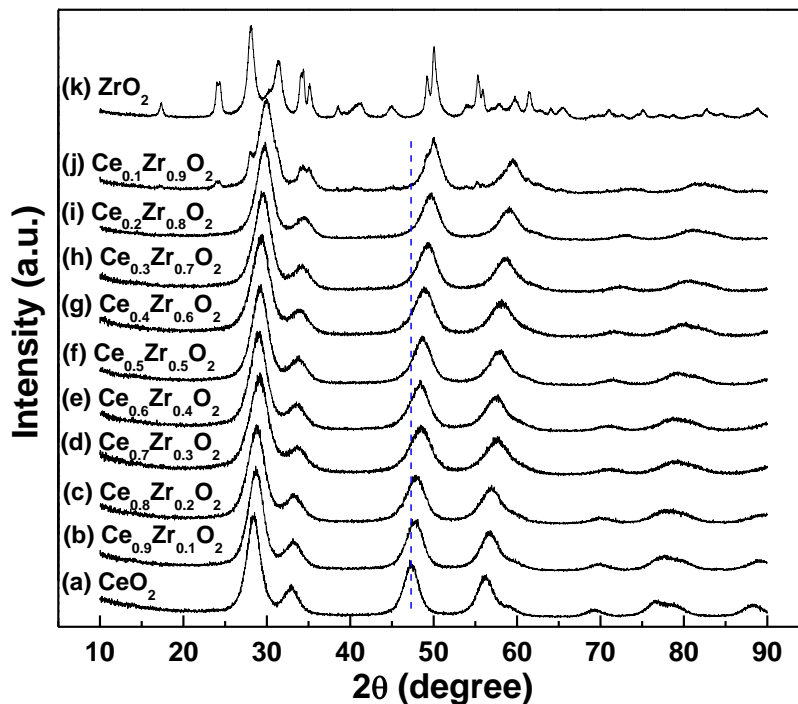
Figure 2. X-ray diffraction patterns of $Ce_xZr_{1-x}O_2$ (0≤x≤1) nanocrystals via a one-step hydrothermal reaction at 150 °C for 48 hrs.

Table 1 compares BET surface area, the crystalline size, and lattice parameter between pure CeO_2 or ZrO_2 and $Ce_xZr_{1-x}O_2$ (0<x<1) mixed oxides. Monoclinic ZrO_2 shows the lowest BET surface area, much higher crystallinity, and larger crystalline size. It is noted that the obtained ZrO_2 presents a monoclinic structure after hydrothermal processing at 150°C without containing hydroxide phase (i.e, $Zr(OH)_4$) in the strong base solution environment (6M NaOH), so no further decomposition step is necessary to form zirconium oxide (ZrO_2) nanocrystals. Direct formation of zirconium oxide is one of the advantages for hydrothermal reaction, in comparison with the initial formation of zirconium hydroxide in other chemical methods using a base solution ($NH_3 \cdot H_2O$ or NaOH). Also unlike other metal oxides (Al_2O_3, Fe_2O_3, Co_3O_4, NiO, PrO_2, TbO_2), hydroxides (γ-AlO(OH), FeO(OH), $Co(OH)_2$, $Ni(OH)_2$, $Pr(OH)_3$, $Tb(OH)_3$) forms preferably under strong base conditions during hydrothermal reaction. Therefore, the direct formation of ZrO_2 nuclei under hydrothermal reaction may facilitate the formation of $Ce_xZr_{1-x}O_2$ (0<x<1) as solid solution process between CeO_2 and ZrO_2 proceeds in a liquid phase environment under pressure. The highest BET surface area obtained is from pure CeO_2 (153.74

m^2/g), and the mixed oxides show a little lower BET surface area (108~143 m^2/g) which is higher than the reported values in other works using co-precipitation and sol-gel methods. The mixed oxides show on average a little smaller particle sizes than that of pure CeO$_2$. Table 1 also shows the relationship between ZrO$_2$ content and the lattice parameter of all Ce$_x$Zr$_{1-x}$O$_2$ (0≤x≤1) nanocrystals samples, calculated using the (111) peak. The calculated lattice parameters for the Ce$_x$Zr$_{1-x}$O$_2$ (0≤x≤1) nanocrystals follow the same trend with the XRD results, indicating a decreased lattice parameter and unit cell volume as the ZrO$_2$ concentration increases.

Table 1. BET surface area, crystalline size, and lattice parameters of the Ce$_x$Zr$_{1-x}$O$_2$ (0≤x≤1) nanocrystals

Sample Composition	BET Surface Area (m^2/g)	Crystalline Size from XRD (nm)	Lattice Parameter (Å)
ZrO$_2$	23.52	20.2	a:5.156;b:5.191;c:5.304
Ce$_{0.1}$Zr$_{0.9}$O$_2$	108.33	3.7	a:5.196;b:5.196;c:5.237
Ce$_{0.2}$Zr$_{0.8}$O$_2$	112.34	4.0	5.249
Ce$_{0.3}$Zr$_{0.7}$O$_2$	108.07	3.7	5.278
Ce$_{0.4}$Zr$_{0.6}$O$_2$	121.03	3.5	5.299
Ce$_{0.5}$Zr$_{0.5}$O$_2$	113.31	3.5	5.318
Ce$_{0.6}$Zr$_{0.4}$O$_2$	118.93	3.7	5.362
Ce$_{0.7}$Zr$_{0.3}$O$_2$	120.46	3.3	5.381
Ce$_{0.8}$Zr$_{0.2}$O$_2$	114.97	3.7	5.416
Ce$_{0.9}$Zr$_{0.1}$O$_2$	142.85	3.9	5.430
CeO$_2$	153.74	4.6	5.446

The TEM images with the selected compositions (Ce$_{0.7}$Zr$_{0.3}$O$_2$, Ce$_{0.5}$Zr$_{0.5}$O$_2$, and Ce0$_{.3}$Zr$_{0.7}$O$_2$) are shown in Figure 3. The TEM analyses confirmed that the size of nanocrystals is in the range of 3-5 nm in diameter with single crystal characteristic. It seems that a morphological change of nanocrystals occurs from irregular shape with well-defined crystal facets to round shape as the ZrO$_2$ concentration increases. HRTEM image of the Ce$_{0.7}$Zr$_{0.3}$O$_2$ sample (Figure 3-a-2) clearly display a faceted surface terminated by the atomic-level lattice fringes. Due to the low scattering power of oxygen when compared with heavy cerium, the dark contrast (black spots) in the HRTEM images (Figure 3) is presumed to be a terminating layer of cerium cations. Analysis of the images showed that these facets/edges terminate in {111} and {200} planes, based on their d-spacing and the corresponding diffractogram. For the Ce$_{0.3}$Zr$_{0.7}$O$_2$ sample, the atomic-level surfaces are relatively rough and the particle morphology eventually changes to round shape, which is clear in the low-magnification image (Figure 3-c-1). This observation of morphology change might be related to the structure transformation from cubic to tetragonal with the increased ZrO$_2$ concentration illustrated in the CeO$_2$-ZrO$_2$ phase diagram.
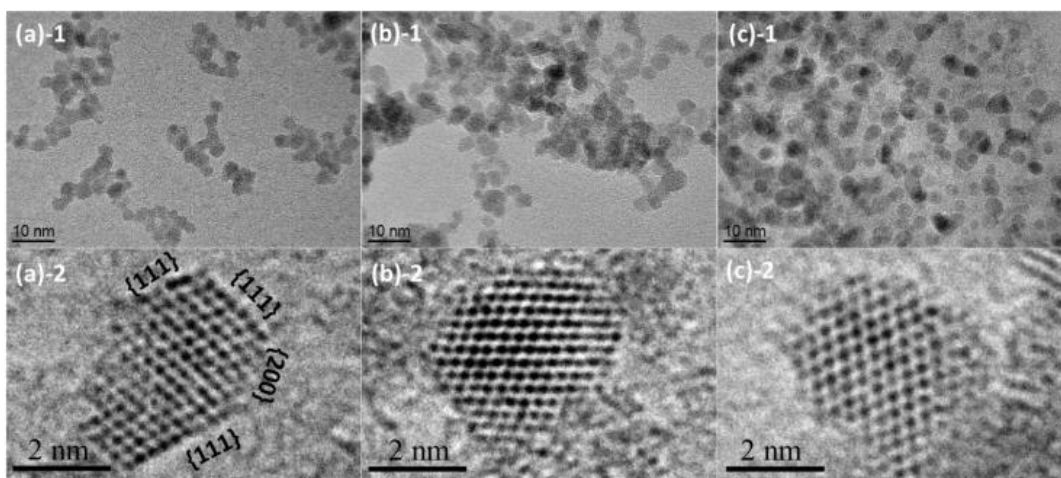
Figure 3. Representative TEM and HRTEM images of $Ce_{0.7}Zr_{0.3}O_2$ (a-1/2), $Ce_{0.5}Zr_{0.5}O_2$ (b-1/2), and $Ce_{0.3}Zr_{0.7}O_2$ (c-1/2) nanocrystals prepared by hydrothermal reaction at 150 ^{o}C for 48 hrs with a 40 mins stirring treatment in air.

It should be pointed out that all $Ce_xZr_{1-x}O_2$ ($0 \leq x \leq 1$) samples, reported in Figure 2 and Table 1, were stirred on a magnetic hot plate for 40 mins at room temperature before the hydrothermal reactions. It was found that the stirring step was playing a critical role in the control of compositional homogeneity, particle size, and morphology of final products. For example, for pure CeO_2, nanocubes with a size of 20 nm was obtained without initial stirring, but irregular shape nanocrystals with much smaller particle size (4~5 nm) were obtained if stirring the mixture of $Ce(NO_3)_3$ and NaOH for 40 mins before loading into the autoclave reactor, as shown in TEM images of Figure 4 (a-1 and b-1). HRTEM images and the corresponding fast Fourier transform (FFT) diffractograms are shown in Figure 4 a-2 and b-2 in order to study the detailed crystalline feature of such polyhedral nanocrystals. The inserted diffractorgrams confirm the cubic (or psudocubic) structure and single crystal characteristics of nanocrystals, and the HRTEM images show the dominant {111} surface facets for irregular particles for the stirred samples and {200} surface facets for the nanocubes in the unstirred samples.
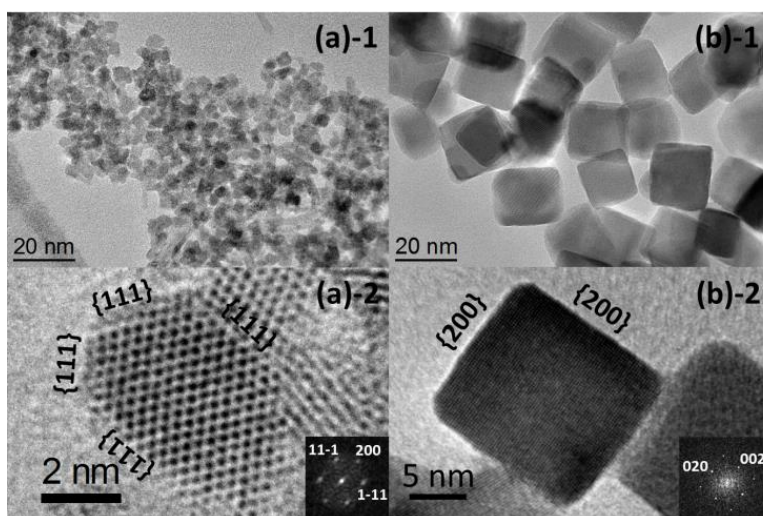
Figure 4. TEM images of CeO_2 nanocrystals prepared by hydrothermal reaction at 150 ^{o}C with (a) and without (b) stirring treatment.

Effect of stirring on the formation of solid solutions

Figure 5 compares the XRD results of the $Ce_{0.7}Zr_{0.3}O_2$, $Ce_{0.3}Zr_{0.7}O_2$ and $Ce_{0.5}Zr_{0.5}O_2$ samples with and without stirring treatment before loading to the autoclave for hydrothermal reaction. For the stirred samples, it is found that {111} diffraction peak at about 29° in the patterns shifts to higher diffraction angle with increasing ZrO_2 concentration. This indicates a decrease in unit cell volume due to the incorporation of smaller Zr^{4+} ions into lattice positions. For the unstirred samples, the phase separation occurs for the $Ce_{0.7}Zr_{0.3}O_2$, although $Ce_{0.3}Zr_{0.7}O_2$ and $Ce_{0.5}Zr_{0.5}O_2$ samples show an apparently compositional homogeneity.
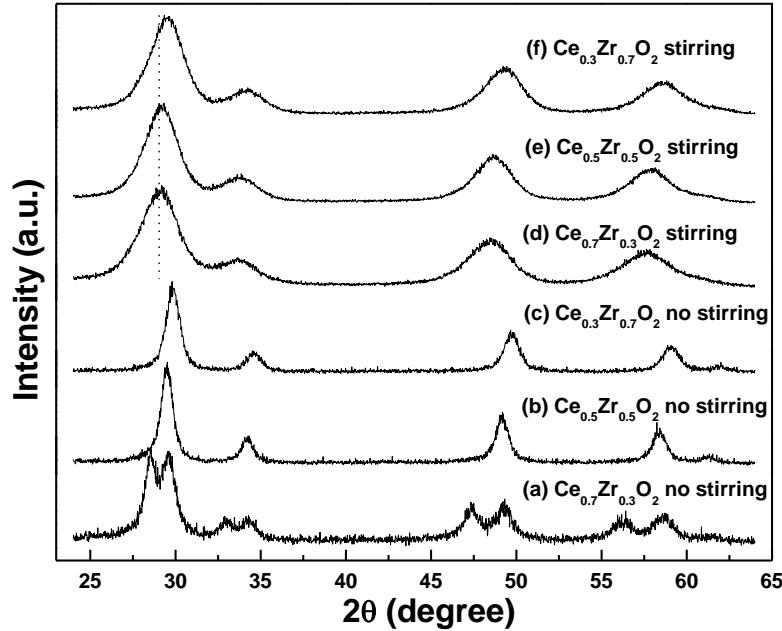
Figure 5. XRD patterns of $Ce_{0.3}Zr_{0.7}O_2$, $Ce_{0.5}Zr_{0.5}O_2$, and $Ce_{0.7}Zr_{0.3}O_2$ mixed oxides showing the effect of stirring treatment before hydrothermal reaction on the compositional homogeneity of final products.

To gain further insights into the role of the stirring on the synthetic process of CeO_2-ZrO_2 solid solutions, a possible formation mechanism of $Ce_xZr_{1-x}O_2$ (0<x<1) mixed oxides nanocrystals from metal nitrate solution and NaOH is proposed as follows: First, the hydrated metal ions are hydrolyzed to metal hydroxides (Step 1 and 2: $ZrO(OH)_2$ and $Ce(OH)_3$) when mixing metal nitrate with NaOH. The metal hydroxides are not stable under high pressure during the hydrothermal reaction at 150^oC. Then, metal hydroxides proceed to precipitate as metal oxides through dehydration and oxidation (Step 3).

$$ZrO(NO_3)_2 + 2NaOH \rightarrow 2NaNO_3 + ZrO(OH)_2 \quad (1)$$

$$Ce(NO_3)_3 + 3NaOH \rightarrow 3NaNO_3 + Ce(OH)_3 \quad (2)$$

$$4(1-x)ZrO(OH)_2 + 4xCe(OH)_3 + xO_2 \xrightarrow{T,\ P} 4Ce_xZr_{1-x}O_2 + 2(x+2)H_2O \quad (3)$$
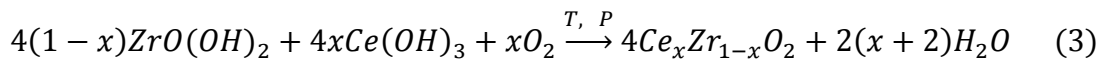
It is interesting to compare the formation of Ce-rich ($Ce_{0.7}Zr_{0.3}O_2$) and Zr-rich ($Ce_{0.3}Zr_{0.7}O_2$) solid solutions from an aqueous solution. The observation shown in Figure 5 gives

insight about the formation of the oxide solid solutions. For the unstirred samples, a compositionally homogeneous $Ce_{0.3}Zr_{0.7}O_2$ solid solution can form under hydrothermal reaction at 150 ^{o}C, but the phase separation occurred for the $Ce_{0.7}Zr_{0.3}O_2$ sample. This seems to indicate that high CeO_2 or $Ce(OH)_3$ concentration does not favor the formation of CeO_2-ZrO_2 solid solution. In other words, the result may suggest that ZrO_2 or $ZrO(OH)_2$ nuclei works as centers of solidification process, by Ce-rich component dissolving in Zr-rich component under hydrothermal reaction conditions. Without stirring, the solid solution process was limited, resulting in a phase separation for the high cerium concentration samples. When stirring was applied, the product obtained showed a compositional homogeneity for all three samples. *It indicates that the stirring treatment promotes the "solid solution" formation, which could be due to the increased diffusion rate and collision between metal hydroxides nucleus by stirring.*

This hypothesis seems supported by our TEM investigation, shown in Figure 6. Figure 6 shows the representative TEM images for the $Ce_{0.7}Zr_{0.3}O_2$, $Ce_{0.5}Zr_{0.5}O_2$, and $Ce0_{.3}Zr_{0.7}O_2$ nanocrystals prepared by hydrothermal reaction at 150 ^{o}C for 48 hrs without 40 mins pre-stirring in air. The $Ce_{0.5}Zr_{0.5}O_2$ and $Ce0_{.3}Zr_{0.7}O_2$ samples show uniform size and shapes of nanoparticles. The morphological heterogeneity was only found for the sample of $Ce_{0.7}Zr_{0.3}O_2$, with a mixed morphology of nanorods and irregular shape nanoparticles. EDX analysis shows that the nanorods is a Ce-rich phase (x>0.5 in $Ce_xZr_{1-x}O_2$). Therefore an intimate and homogeneous contact of cerium and zirconium precursor is particularly important to form a homogeneous ceria zirconia solid solution, which is the reason we mixed all of solid solution precursors for 40 mins before the hydrothermal reactions in the systematic study of $Ce_xZr_{1-x}O_2$ (0≤x≤1).
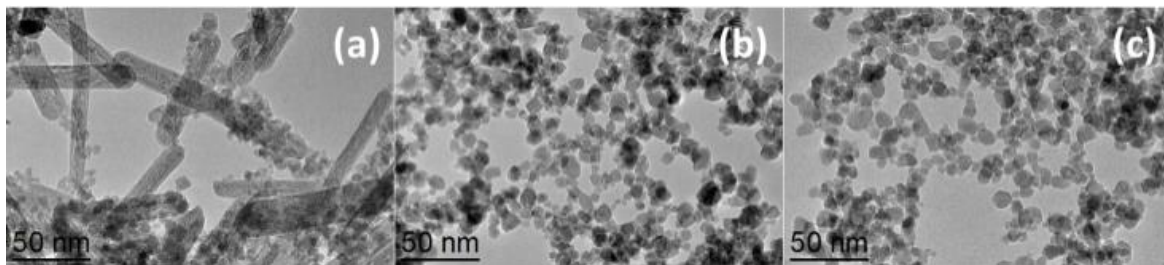
Figure 6. Representative TEM images of the $Ce_{0.7}Zr_{0.3}O_2$ (a), $Ce_{0.5}Zr_{0.5}O_2$ (b), and $Ce0_{.3}Zr_{0.7}O_2$ (c) nanocrystals prepared by hydrothermal reaction at 150 ^{o}C for 48 hrs without the 40-minute stirring treatment in air.

Raman spectroscopy study

The Raman spectra of $Ce_xZr_{1-x}O_2$ (0≤x≤1) nanocrystals are compared in Figure 7. The Raman-active modes in pure CeO_2 are well characterized by the 458 and 605 cm^{-1} bands, and are attributed to a symmetrical stretching F_{2g} mode of the Ce-O8 vibrational unit. The Raman spectrum of pure monoclinic ZrO_2 exhibits ten prominent bands in the range of between 300 and 1000 cm^{-1}, including four major bands that are 347, 381, 476, and 614 cm^{-1}, and six weak bands at 306, 333, 504, 538, 558, and 631 cm^{-1}. The Raman bands at 306, 347, 476, 558, 631cm^{-1} are assigned to A_g mode, and the bands at 333, 381, 504, 538, 614 cm^{-1} are assigned to B_g mode in monoclinic ZrO_2. As the ZrO_2 concentration is increased from 0 to 1, the F_{2g} mode frequency exhibits a continuous shift and approaches that of pure CeO_2. The vibration bands are increasingly broader as ZrO_2 composition increases in the $Ce_xZr_{1-x}O_2$ (0≤x≤1) nanocrystals. Raman spectroscopy has a high sensitivity to unit cell distortions and elemental coordination environments, and both ceria and ceria zirconia have been extensively characterized using this

method. Several researchers have employed Raman spectroscopy to study doped ceria/zirconia systems and it has been successfully used to determine the phase composition in the complex ceria zirconia system. According to the phase diagram of the CeO_2-ZrO_2 system, determined from Raman and X-ray diffraction techniques, in whih cubic, monoclinic and tetragonal phases occur. Due to the size of the $Ce_xZr_{1-x}O_2$ ($0 \leq x \leq 1$) nanocrystals obtained, the bands are relatively broad in this study, however, on the other hand it may demonstrate the advantages of hydrothermal synthesis at such low temperature (150 ^{o}C) to prepare mixed oxides with superior compositional homogeneity.
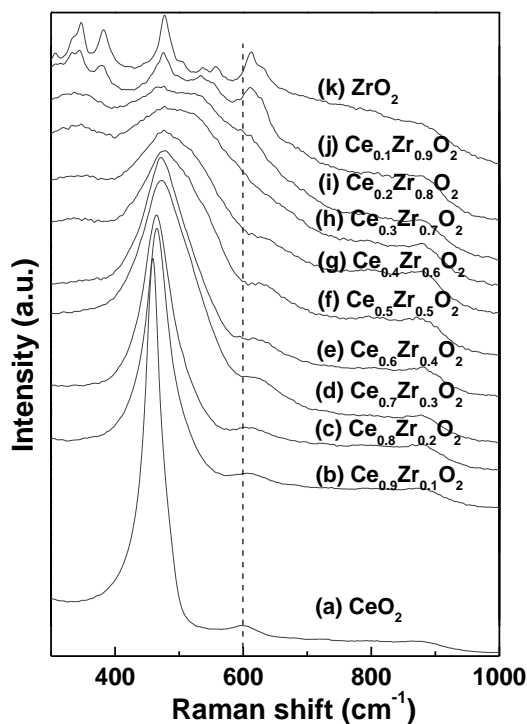
Figure 7. Raman spectra of $Ce_xZr_{1-x}O_2$ ($0 \leq x \leq 1$) nanocrystals.

H$_2$-Temperature programmed reduction (H$_2$-TPR)

Figure 8 shows H$_2$-TPR profiles of $Ce_xZr_{1-x}O_2$ ($0 \leq x \leq 1$) nanocrystals. In pure CeO_2, the H$_2$-TPR profile shows two major reduction peaks corresponding to the surface and bulk reductions, respectively, which are characteristics of reduction temperature and the distribution between the surface and bulk reduction percentage. The coordinately unsaturated surface capping oxygen ions can be easily removed in the low temperature region. However, bulk oxygen requires to be transported to the surface before their reduction. Consequently, the bulk reduction takes place at higher temperature compared to the surface reduction. For pure ZrO_2 nanocrystal, the profile is relative flat, which indicates only a small quantity of H$_2$ was consumed or absorbed on *pure ZrO_2*.

Similar H$_2$-TPR results were obtained over $Ce_xZr_{1-x}O_2$ ($0<x<1$) mixed oxide nanocrystals. Unlike the two surface/bulk reduction peaks in pure CeO_2, only single H$_2$ consumption peak was observed for $Ce_xZr_{1-x}O_2$ ($0<x<1$) mixed oxides. This result clearly shows an improved low-temperature activity in $Ce_xZr_{1-x}O_2$ ($0<x<1$) compared to pure CeO_2. This is consistent with the literature that the reduction peak of CeO_2 shifted to lower temperature by

zirconium addition. One possible explanation for this is that oxygen defects are made in the CeO_2-ZrO_2 solid solution by the existence of zirconium and it is inferred that mobility of oxygen becomes higher, and then the rate of redox reaction becomes faster.
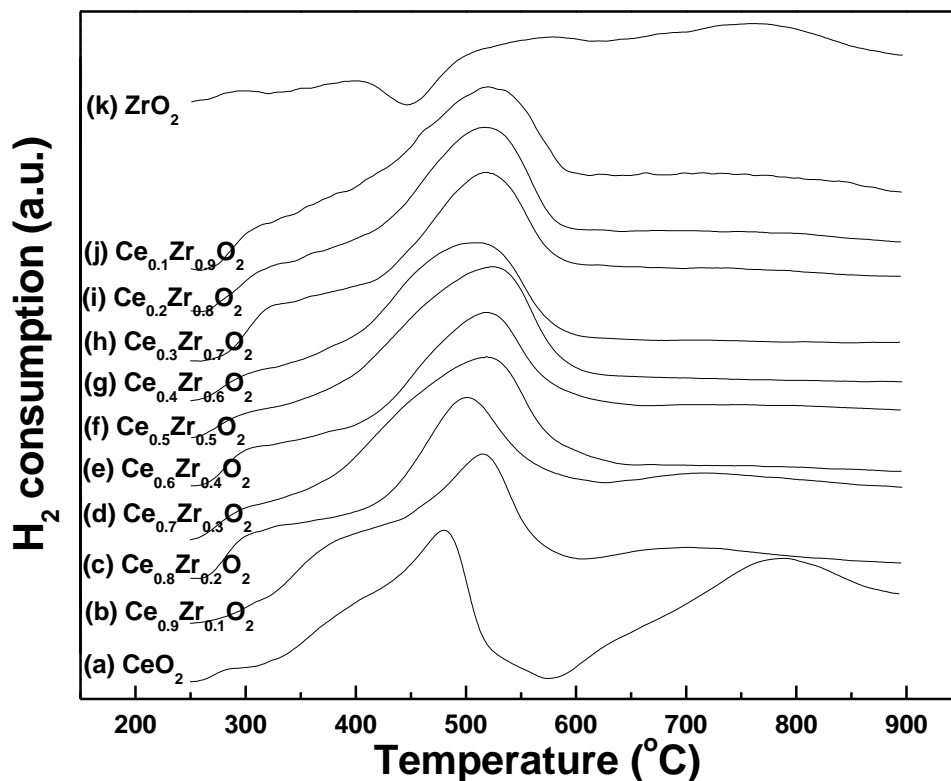
Figure 8. H_2-TPR profiles of $Ce_xZr_{1-x}O_2$ ($0 \leq x \leq 1$) nanocrystals.

Thermal stability under reduction/oxidation conditions

Hydrothermal synthesis, which uses hot pressurized water for precipitation of oxides, is a low temperature and high pressure method. The reaction of the solid solution formation is not under a thermodynamic equilibrium condition, compared to the high temperature solid phase sintering method. In order to evaluate the thermal stability the nanoparticles obtained, Figure 8 shows the XRD patterns for the $Ce_{0.5}Zr_{0.5}O_2$ sample during the thermal treatments under oxidizing (in air) and reducing atmosphere (5%H_2/95%N_2) with an increasing temperature from 900°C to 1400°C. Under reducing atmosphere, at lower treatment temperatures (900°C and 1000°C), the XRD patterns shown in Figure 9 a and b exhibit all the characteristic reflections corresponding to the fluorite-type CeO_2 (JCPDS 34-0394), and the peaks grow narrower and sharper at higher temperatures, indicating crystallite size growth. As the temperature increased above 1100°C, the extra diffraction peaks were observed suggesting that cation order occurs to form pyrochlore-type $Ce_2Zr_2O_{7+x}$ ($0 \leq x \leq 1$) phase, which is similar to our and others' observation. Under oxidizing atmosphere, above 1200°C, phase separation occur in which (200) (~32°) and (220) (49°) peak splitting can be found upon the formation of tetragonal phases. Figure 10 shows the schematic about the transformation from psudocubic to pyrochlore and the psudocubic to tetragonal structure under reduction and oxidation atmosphere, respectively.
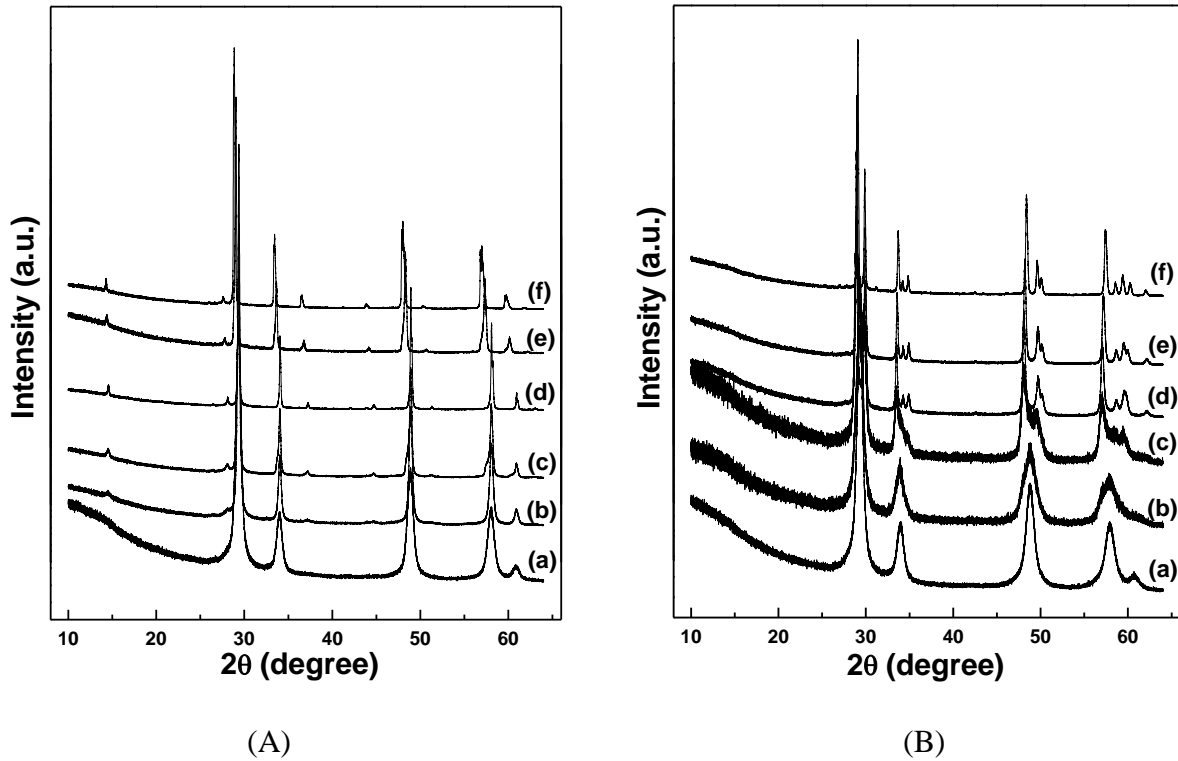
Figure 9. Effects of increasing thermal treatment temperature on the phase homogeneity of $Ce_{0.5}Zr_{0.5}O_2$ samples under oxidizing (A) and reducing atmosphere (B): (a) 900 °C; (b) 1000 °C; (c) 1100 °C; (d) 1200 °C; (e) 1300 °C; (f) 1400 °C.
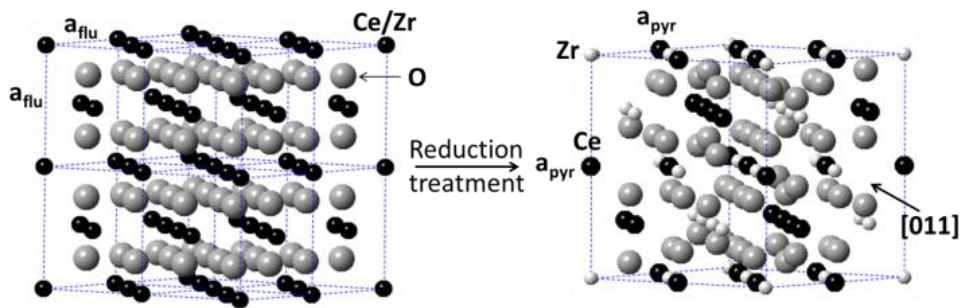
(a) under reducing atmosphere
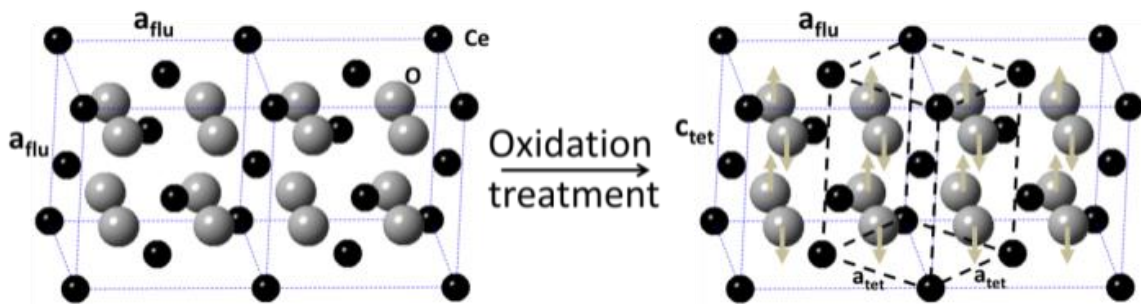
(b) under oxidizing atmosphere

Figure 10. Schematic of structural transformation in $Ce_{0.5}Zr_{0.5}O_2$ during high temperature thermal treatments under reducing and oxidizing atmospheres.

3. Student Researchers Involved in This Grant:

Name (s)	Affiliation	Job Description
Samuel Mutinda (MS graduate)	YSU, Chemistry	Catalytic activity and surface analysis of materials and heterogeneous catalysts
Keyona R.L. Woods	High School Student	solution based oxide nanomaterials synthesis and characterization
Zach Brown (Undergraduate)	YSU, Chemistry	solution based oxide nanomaterials synthesis and characterization

Figure 11. YSU summer nanomaterials program 2011 participants in Dr. Ruigang Wang's research group (from left to right: Zachary Brown, Keyona Rochelle Lynn Woods, and Samuel I. Mutinda). This summer program was supported in part by DoT-CTME project.

4. Listing of Journal Publications and Conference Presentation Resulting from This Grant

- R. Wang, S. Mutinda, Minghao Fang, One-pot synthesis and high temperature thermal stability in $Ce_xZr_{1-x}O_2$ nanocrystals, ***RSC Advances***, 3(42): 19508-19514 (2013)
- R. Dangerfield, D. Li, R. Wang, Low-temperature CO conversion on 1wt%Pt/CeO$_2$ nanocrystals, **Microsc Microanal** 19(Suppl 2): 1700-1701 (2013)
- R. Wang, V. Sama, D. Li, S.I. Mutinda, Hydrothermal synthesis of rare-earth oxide nanocatalysts for automotive exhaust clean-up, ***Advanced Materials Research***, 512-515: 1624-1629 (2012)
- R. Wang, S.I. Mutinda, D. Li, Size/shape-controlled synthesis and low-temperature reactivity of ceria, **Microsc Microanal** 18(Suppl 2): 1394-1395 (2012)
- R. Wang, M. Fang, Improved low-temperature reducibility in ceria zirconia nanoparticles by redox treatment, ***J. Mater. Chem.***, 22: 1770-1773 (2012)